Fe-Single-Atom Catalyst Nanocages Linked by Bacterial Cellulose-Derived Carbon Nanofiber Aerogel for Li-S Batteries

Xueyan Lin[1], Wenyue Li[2], Vy Nguyen[3], Shu Wang[4], Shize Yang[5], Lu Ma[6], Yonghua Du[6], Bin Wang[3], and Zhaoyang Fan[2]*

[1]School for Engineering of Matter, Transport & Energy, Arizona State University, Tempe, Arizona, 85281, USA

[2]School of Electrical, Computer and Energy Engineering, Arizona State University, Tempe, AZ 85281, USA

[3]School of Sustainable Chemical, Biological and Materials Engineering, University of Oklahoma, Norman, OK 73019, USA

[4]College of Health Solutions, Arizona State University, Phoenix, AZ 85004, USA

[5]Eyring Materials Center, Arizona State University, Tempe, AZ 85281, USA

[6]National Synchrotron Light Source II, Brookhaven National Laboratory, Upton, NY, 11973, USA

*Email: zyfan@asu.edu

Abstract

Li-S battery (LSB) is promising for achieving high capacity. Still, its development is hindered by the complex redox process with sluggish kinetics and particularly the resulting lithium polysulfides (LiPS) shuttle effects. Single-atom catalysts (SACs), with their maximized atom utilization, could effectively chemisorb soluble LiPSs and expedite the sulfide conversion reaction kinetics. Here we report incorporating Fe single metal atom catalyst (Fe-SAC) in the sulfur cathode design and its electrocatalytic effects. Fe-doped ZIF-8 nanocages were introduced into a cheap biomass bacteria cellulose. A pyrolysis process converted them into an aerogel structure with Fe-SAC-functionalized N-doped carbon nanocages linked by a carbon nanofiber network (FeSA-NC@CBC), which was applied as a scaffold to fabricate freestanding and binder-free sulfur cathodes. We conducted electrochemical measurements to reveal Fe-SAC functions including lowering energy barriers for S_8 reduction to liquid-phase LiPSs and further to solid-phase Li_2S_2/Li_2S and accelerating Li_2S_2/Li_2S nucleation and deposition, as corroborated by our theoretical calculation results. Benefiting from the synergistic effects of highly active Fe-SAC and three-dimensional conductive network, the sulfide reaction kinetics is improved, which can diminish LiPS shuttle effects and therefore improve LBS rate performance and cycling stability. Accordingly, the fabricated FeSA-NC@CBC composite cathode delivers an excellent rate capability at 2C with a reversible capacity of 840 mAh/g and a long-term cyclic stability of 800 mAh/g at 1C after 500 cycles.

Keywords: Single atom catalyst; metal organic framework (MOF); sulfide reaction kinetics; bacterial cellulose; Li-S battery

Introduction

With sulfur's superior theoretical specific capacity (1675 mA h g^{-1}) and its low cost, the lithium-sulfur battery (LSB) is considered as a promising candidate for next-generation secondary batteries[1]. Despite decades of effort, the development of LSBs still faces significant challenges[2]. In particular, due to the highly electronic and ionic insulating nature of S_8 and Li_2S, the electron/charge transfer inside cathode is greatly retarded during charge/discharge, which seriously restricted the sulfur utilization and rate capability of LSBs. On the other hand, the huge variation upon cycling owing to the mass density difference between sulfur and Li_2S results in expansion stress, which can easily induce cracks or pulverizations in conventional solid sulfur-carbon composite cathodes. Therefore, catholyte chemistry with highly conductive self-standing and binder-free host matrix is favorable for LSB design, in which lithium polysulfides (LiPS) are dissolved so that the electrolyte can access the freshly exposed S_8 during discharge or Li_2S_2/Li_2S during charging and allows homogeneous dispersion of sulfur. This enables a solid-liquid-solid conversion and therefore overcomes the otherwise extremely slow kinetics in a pure solid-solid reaction[3]. However, due to the sluggish redox kinetics of the intermediate LiPSs, if the LiPSs cannot not be effectively confined and rapidly to converted solid Li_2S_2/Li_2S products inside the cathode, they can diffuse out of the cathode and penetrate the separator to react with the Li metal anode[4, 5], leading to irreversible electrode degradation and interior cycling lifespan, which is a major challenge for LSB technology known as 'shuttle effect'[6].

To address the challenges, the use of conductive, porous, and heteroatom-doped carbon matrices as sulfur hosts has been widely reported[7-9]. While this strategy has brought about significant progress, a practical solution is still elusive. With the understanding of the solid-liquid-solid conversion process in the sulfur cathode and recognition of the sluggish reaction kinetics limited by large energy barriers[10], various transition metal-based electrocatalysts have been investigated to promote the redox reaction of sulfides[11, 12]. Apart from the established research that has disclosed traditional oxide and nitrite catalysts to enhance the performance and stability of Li-S batteries[13, 14], recent studies have ventured into exploring selenide and boride catalysts [15-17] and complicated phase transitions within various transition-metal compounds

to address the inherent limitations in conductivity and thus boost catalytic activity[18-20]. These catalytic materials are typically loaded in a carbon matrix as nanoparticles, which can chemically bind LiPS and accelerates their conversion kinetics[21, 22], resulting in improved battery performance. However, these transition metal-based catalysts are heavy and have feature sizes at tens or even hundreds of nanometers with a low density of surface-active sites. The large amount incorporation required to achieve sufficient efficiency further reduces the already low sulfur fraction in the cathode, sacrificing the overall energy density and competitiveness of LSBs compared to lithium-ion batteries (LIBs)[23, 24]. Besides, downsizing the particles is conducive to providing full access to electrochemical interfaces and smooth electron/ion pathways. Therefore, the employment of single metal atoms in sophisticated electrode design is highly desirable.

Atomic-scale single-atom catalysts (SACs) are gaining significant attention due to their unique properties. Commonly, SACs based on transition metals are fabricated by coordinating metal atoms on N-doped graphitic surfaces to form M-NC structures. These SACs offer a theoretical 100 % atom utilization, abundant active sites, and therefore possess a much higher catalytic efficiency than conventional bulk metal and nanoparticle catalysts[25, 26], making them ideal for various electrochemical reactions with exceptional activity and selectivity[27, 28]. Recently, there has been growing interest in incorporating SACs in the sulfur cathode design[29-32], as they are believed to chemisorb LiPS and catalyze their conversion into Li_2S and vice versa, thereby improving the reaction kinetics and reducing energy barriers even with a low SAC mass loading. Recently, d-p orbital hybridization between SACs and sulfur species was proposed as a descriptor to explain the SAC mechanisms in LSBs. The strong hybridization can (i) effectively bind Li_2S and soluble LiPSs, (ii) make dissociation of S–S bonds easier in the sulfur chain and promote LiPSs reduction, and (iii) weaken Li–S bonds in the Li_2S cluster and thus reduce the energy barrier to Li_2S oxidation[33]. Hence, researching the roles of SACs in promoting sulfur redox reactions in Li-S chemistry and their incorporation in the cathode structure is significant and holds great potentials.

Pyrolysis is a commonly used method to synthesize SACs on carbon substrates[33], and metal organic frameworks (MOFs) are ideal precursors for pyrolysis by leveraging the atom spatial confinement function

within MOF cages[34]. This is particularly true for metal-doped zeolitic imidazolate framework-8 (M-ZIF-8) that contains abundant nitrogen element. During the pyrolysis process, the ligands of the ZIF-8 organic framework are removed and the metal (M) element with low vapor pressure substitutes Zn to attain M-NC moieties with atomic distribution by being coordinated with substitutional nitrogen (N) atoms in the graphene (C) lattice. The nanocage architecture of MOF could further encapsulates and isolates the metal ions from clustering[35]. The formed porous carbon nanocage structure exposes and makes the SACs accessible, while also trapping dissolved LiPSs[36]. N-rich MOF-derived carbon anchored with a single iron atom (FeSA-NC) has been recently demonstrated to effectively improve the kinetics of LiPSs conversion reaction and enhance the performance of LSBs[37].

The reported SACs in literature are commonly synthesized as powder, which are mixed with sulfur, conductive agents, binders, and solvents to form a paste for slurry-coating on aluminum foil, following the conventional powder-based cathode design. A freestanding cathode structure offers advantages over this design. Bacterial cellulose (BC) is a natural biomass material with a three-dimensional (3D) network structure interweaved by numerous nanofibers[38]. Carbonized bacterial cellulose (CBC) has been investigated for multiple electrochemical applications[39], particularly as a freestanding and flexible sulfur host[40], as it enables current collector and binder-free fabrication[40], which can further increase the energy density and reduce the interfacial resistance. It is further noted that the presence of numerous hydroxyl groups on BC macromolecules facilitates the nucleation and growth of nanocrystals on the BC nanofibers and avoids aggregation[41].

Herein, we report our investigation of atomically distributed Fe on N-doped graphitic surfaces and their catalytic effects in Li-S chemistry. In addition to FeSA–NC nanocages derived from Fe-doped ZIF-8 powder, we synthesized Fe-doped ZIF-8 directly inside BC *in situ* with controlled ZIF-8 crystal particle size. A pyrolysis process carbonized BC into 3D conductive aerogel, with ZIF-8 derived FeSA-NC nanocages anchored on the conductive carbon nanofibers. We utilized this FeSA-NC@CBC aerogel as the host to fabricate freestanding sulfur cathodes and investigate the catalytic functions of FeSA-NC in promoting the S_8-LiPs-Li_2S conversion to address the LiPS shuttling problem. In consistency with DFT-

based calculation, significantly improved LSB performance was confirmed through our experiments. The 3D interconnected fibrous networks with hierarchical porosity ensure efficient electrical charge transfer and buffer the volume variation during cycling. Coupled with the synergistic effects of highly active Fe-SAC to effectively chemisorb LiPSs and expedite the redox conversion kinetics, the Li–S batteries assembled with such self-standing and binder-free electrocatalytic cathodes deliver a superior rate capability of 840 mAh g^{-1} at a high current density of 2C and a low-capacity decay rate of 0.042% per cycle after 500 cycles at 1C.

Results and Discussion

Material synthesis and characterization

The overall material preparation process is schematically shown in **Fig. 1(a)** and the material changes after each step are depicted in **Fig. 1(b)** through digital photos. Initially, BC was impregnated into a methanolic solution containing Fe salts and ZIF-8 precursor for adsorption. The functional groups on the BC nanofibers facilitated the growth and dispersion of ZIF-8 nanocrystals along the fiber surface in a solvothermal process. During the formation of ZIF-8 nanocages, the individual Fe ions were spatially isolated and encapsulated. Subsequently, the mixture underwent freeze-drying and pyrolysis, resulting in ZIF-8-derived graphite-like carbon serving as the substrate, with isolated single Fe atoms anchored and stabilized on the carbon substrates through coordination with N atoms. This process yielded a porous structure that enabled efficient mass transfer and physical confinement of sulfur species. As illustrated in **Fig. 1(a)**, the Fe SAC (single atom catalyst) was atomically dispersed on the nanocage surface, chemically trapping the LiPS through strong interaction. Subsequently, the Fe-SAC accelerated the conversion of LiPS to Li_2S by lowering the energy barrier, thereby suppressing the diffusion of LiPS (i.e., shuttle effect)[42]. Reference samples were made for comparison. N-doped carbon nanocages linked by carbonized bacterial cellulose (NC@CBC) was prepared by replacing Fe-ZIF-8 with bare ZIF-8 via a similar protocol, and a

pure carbonized bacterial cellulose aerogel (CBC) was prepared by direct pyrolysis of BC aerogel without introducing ZIF-8 nanoparticles.

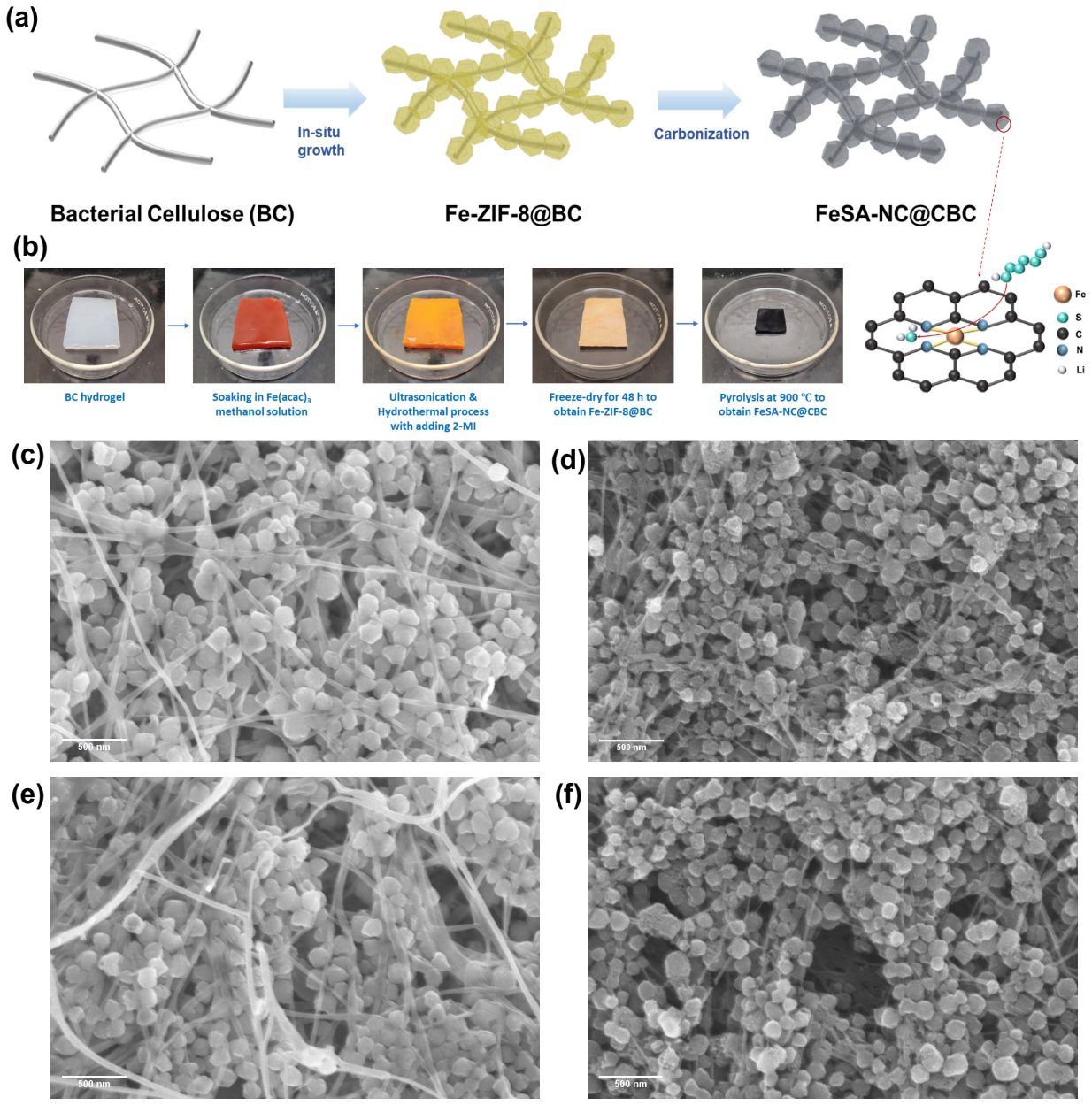

Figure 1 (a) Schematic illustration of the synthesis process of FeSA-NC@CBC. (b) Digital photos of preparation procedures of Fe-ZIF-8@BC and FeSA-NC@CBC composites. SEM images of (c) ZIF-8@BC, (d) NC@CBC, (e) Fe-ZIF-8@BC, and (f) FeSA-NC@CBC, respectively.

A scanning electron microscope (SEM) was utilized to observe the surface morphology and architecture of the nanocage-based composite. As displayed in **Fig. S1(a) and (b**), the carbonized BC (CBC) aerogels retained the 3D network structure of the BC aerogel after pyrolysis at high temperature, in which the nanofibers, with a diameter of a few tens of nm, were interconnected to each other. The branched 3D carbon nanofiber network served as the ideal conductive matrix and current collector for a free-standing sulfur cathode. The free void space in the network helps to accommodate large volume expansion during lithiation process[43]. As shown in **Fig. 1(c) and (e**), ZIF-8 and Fe-ZIF-8 nanocrystals were decorated along the BC nanofibers during in-situ growth, although they tended to accumulate closer to the surface. The prepared ZIF-8@BC and Fe-ZIF-8@BC composites feature the 3D network structure of BC and a typical dodecahedral shape of ZIF-8 nanocrystals. Abundant hydroxyl groups and highly exposed surface area of BC nanofibers facilitate the ZIF-8 nucleation and thus favors the growth of nanocrystals in small size, as well as prevent their agglomeration and clustering. After pyrolysis, as shown in **Fig. 1(d) and (f**), the ZIF-8 and Fe-ZIF-8 derived nanocages (NC and FeSA-NC), with a size of ~ 80 nm, are decorated on the carbon scaffold.

It is crucial to control the size of synthesized FeSA-NC nanocages for obtaining high-quality FeSA-NC@CBC aerogels. Before integrating the FeSA-NC nanocages into the CBC matrix, homogeneous ZIF-8 derived NC cages with different sizes were synthesized by adjusting the reactant/solvent concentration ratio. As displayed in **Fig. S2(a)-(c)**, the size was controlled to be around 40 nm, 80 nm and >500 nm. Those large nanocages (> 500 nm), derived from large ZIF-8 particles as typically reported in the literature, do not fit in the void space of BC during synthesis. On the other hand, when ZIF-8 nanocrystals of ~ 40 nm diameter were synthesized into the BC matrix, ZIF-8 nanoparticles tend to be highly agglomerated rather than uniformly dispersed along the BC nanofibers (**Fig. S3**). Therefore, the size of FeSA-NC nanocages in this work was elaborately selected to be ~ 80 nm, giving a relatively uniform distribution combining with high specific surface area and maximized active sites utilization. A BET analysis is performed to verify the conclusion as shown in **Fig. S4**, the increased surface area and pore volume of 80 nm FeSA-NC@CBC can be attributed to the uniform distribution of FeSA-NC nanocages inside the CBC matrix.

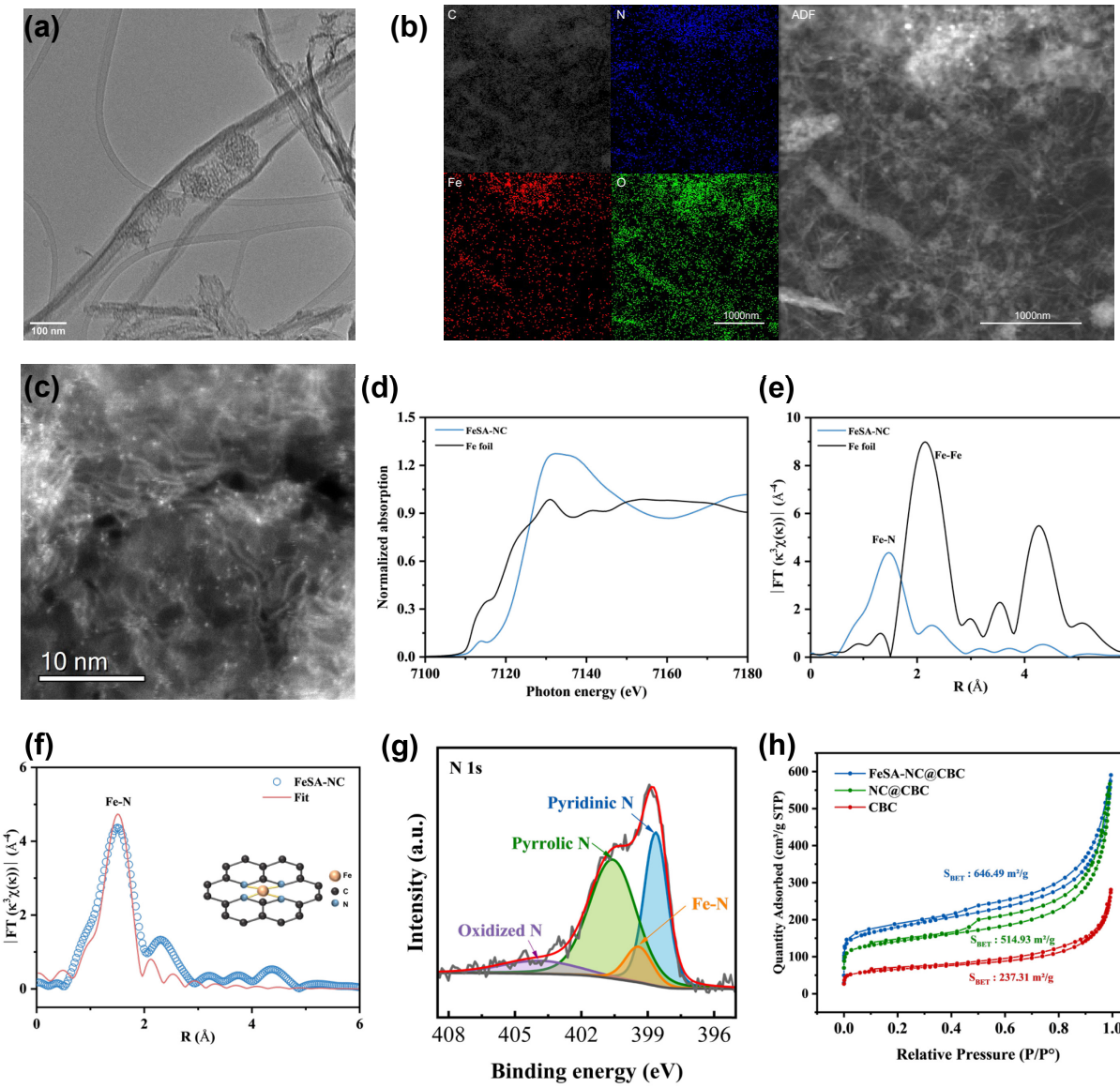

Figure 2 (a) TEM images of FeSA-NC@CBC. (b) ADF-STEM images of FeSA-NC@CBC and its corresponding element maps showing the distribution of C (grey), N (blue), Fe (red) and O (green). (c) AC-HAADF-STEM image of FeSA-NC@CBC. (d)XANES and (e) FT-EXAFS spectra of the FeSA-NC and Fe foil. (f)The corresponding FT-EXAFS fitting curve of FeSA-NC. (g) High-resolution N 1s XPS spectra of FeSA-NC@CBC. (h) N_2 adsorption–desorption isotherm of FeSA-NC@CBC, NC@CBC and CBC.

Transmission electron microscopy (TEM) images revealed more details on the microstructure of FeSA-NC as shown in **Fig. 2(a)** and **Fig. S5 (a, b)**. The FeSA-NC exhibits a porous hollow structure with plenty of micro and

mesopores on its surface. The highly porous structure enables exposed active sites for promoting catalysis efficiency and abundant voids to encapsulate or confine LiPSs species. Moreover, porous texture is expected to shorten the diffusion length of the electrolyte ions. Notably, no aggregated nanoparticles or clusters were observed on the carbon substrate, which is consistent with the X-ray diffraction (XRD) pattern without detecting Fe metallic nanoparticles or nanoclusters diffraction signals shown in **Fig. S9**. The annular dark-field scanning TEM (ADF-STEM) image and its corresponding elemental mapping displayed in **Fig. 2(b)** for FeSA-NC@CBC and **Fig. S6** for FeSA-NC confirmed the existence and distribution of C, Fe, N and O. It is worth noting that the distribution of Fe element almost overlapped with N element, suggesting that the N atoms help to anchor the Fe single atoms in the form of Fe-N coordination. The atomic resolution aberration-corrected high-angle annular dark-field STEM (AC-HAADF-STEM) image shown in **Fig. 2(c)** and **Fig. S5(c)** clearly demonstrates the presence of Fe single atoms, which were observed as isolated bright dots dispersing on the carbon support owing to higher Z contrast of Fe than N and C atoms[44-46]. To further understand the electronic structure and coordination environment of the Fe SACs, the X-ray absorption near-edge structure (XANES) and the extended X-ray absorption fine structure (EXAFS) of FeSA-NC were measured. The XANES spectra in **Fig. 2(d)** manifests a weak peak at ~7113 eV in the pre-edge region. The shift in the absorption edge for FeSA-NC to a higher energy level as compared to that of Fe-foil implying an increase in the oxidation state of Fe. It is assigned to the 1s→ 3d transition along with simultaneous charge transfer of ligand-to-metal, which is regarded as the fingerprint of square-planar Fe–N_4 configuration with a porphyrin-like structure[47]. In the FT-EXAFS spectra presented in **Fig. 2(e)**, an obvious peak at 2.34 Å in Fe foil sample was attributed to the Fe-Fe shell. In contrast, the spectra of FeSA-NC exhibits a primary peak located at ~1.5 Å, corresponding to the Fe–N scattering path[35]. The detailed single atom structural status of Fe SACs obtained via EXAFS fitting was presented in **Fig. 2(f)** and **Table S1**, which elucidates the coordination number is 3.6 ± 0.6 with the Fe-N average distance of 2.01 ± 0.04 Å. Accompanied by the absence of Fe-Fe scattering, it can be concluded that the Fe atom is coordinated by N atoms in the form of Fe-N4 moieties of the Fe center in FeSA-NC[48].

X-ray photoelectron spectroscopy (XPS) was carried out to investigate the chemical information and atomic bonding configuration in the FeSA-NC@CBC sample. The survey plot in **Fig. S7(a)** indicates the presence of carbon

(C), nitrogen (N), oxygen (O) and iron (Fe) and the nitrogen content was found to be 4.6 atom%. The binding states of N, C and Fe in FeSA-NC@CBC were further revealed by high-resolution spectra. The N 1 s spectra in **Fig. 2(g)** can be deconvoluted into four nitrogen species: pyridinic N (398.6 eV), pyrrolic N (400.6 eV), oxidized N (403.9 eV) and N coordinated with Fe single atoms (399.4 eV). Different N dopants embedded in carbon are expected to serve as anchor points for Fe atoms and chemically adsorb LiPSs by modifying the carbon substrates with polar surfaces, which can effectively suppress the shuttle effect and improve sulfur utilization [49]. The Fe 2p XPS spectra presented in **Fig. S7(b)** manifested typical peaks assigned to Fe $2p_{1/2}$ and Fe $2p_{3/2}$ signals, indicating high-valence Fe atoms in a coordination structure rather than aggregated metallic Fe (706.2 eV). The analysis of the overlapping peaks reveals that the two distinct sub-peaks were observed around 709.8 eV and 713.8 eV, which can be attributed to Fe^{2+} $2p_{3/2}$ and Fe^{3+} $2p_{3/2}$, respectively[50]. Moreover, the peak at 711.6 eV was consistent with the binding energy between Fe and N, further confirming the existence of Fe-N active sites[51]. Regarding the high-resolution spectra of C 1s in **Fig. S7(c)** , the graphitized C–C/C=C bonds (284.8 eV), C-N/C-O bonds (285.6 eV) as well as C=O bonds (287.5 eV) were observed [7].

The porous features of the samples were investigated by Brunauer-Emmett-Teller (BET) measurements to determine their specific surface area and pore size distribution. Compared with CBC (237.3 m^2/g), the specific surface area of FeSA–NC@CBC and NC@CBC was significantly increased after adding ZIF-8 derived carbon nanocages (646.5 m^2/g and 514.9 m^2/g, respectively). As depicted in **Fig.2(h)**, the FeSA-NC@CBC shows a typical type IV isotherm which is similar to that of NC@CBC, while the CBC without ZIF-8 derived carbon nanocages manifests a type I isotherm. The higher initial steep adsorption at low P/P^0 (close to 0) indicates the presence of more abundant micropores in FeSA-NC@CBC and NC@CBC compared to CBC. And the hysteresis loop observed at medium P/P^0 proves the existence of mesopores. All three samples were found to have micropores (<5 nm) as in the pore size distribution curves (**Fig. S8**), and FeSA-NC@CBC has the highest pore volume of 0.789 cm^3/g. Clearly, by introducing carbonized ZIF-8 nanocages, a hierarchical micro/mesoporous structure with enlarged surface area was obtained in FeSA-NC@CBC. The mesopores are mainly derived from the evaporation of Zn species[52]. The high pore volume is conducive to accommodate high sulfur loading and large volume variation upon cycling. Specifically, micropores can give a strong physical confinement for LiPSs to alleviate the shuttle effect whilst

mesoporous effectively increase the electrochemical wettability and electrode/electrolyte interfaces[53]. More exposed and accessible Fe SACs active sites facilitate sulfur redox reactions as well as ensuring rapid mass transfer, consequently promoting batteries rate capabilities.

The XRD patterns of Fe-ZIF-8@BC before and after carbonization were displayed in **Fig. S9**. The presence of strong peaks of prepared Fe-ZIF-8@BC composite indicates its high crystallinity. However, after pyrolysis, the XRD patterns of FeSA-NC@CBC mainly showed two broad peaks at around 25° and 45° (2 theta), which are assigned to the (002) and (101) reflection of graphitic carbon with a low degree of graphitization, indicating that these carbonized products have amorphous properties[54, 55]. Based on the XRD spectrum of FeSA-NC@CBC, which did not exhibit the Fe-related crystalline peaks, we further confirmed that the atomically dispersed iron spatial isolation was realized during the preparation process.

Electrocatalytic studies

To catalytically convert the soluble LiPS to Li_2S_2/Li_2S solids, they must first be absorbed on the catalyst surface. We tested the polysulfide adsorption capability of the three samples. FeSA-NC@CBC, NC@CBC, and CBC freestanding scaffolds were placed into a diluted Li_2S_6 solution (0.005 M) for 12 h to observe the color change. As shown in **Fig. 3(a)**, the dark yellow Li_2S_6 solution became transparent after 12 h with FeSA-NC@CBC. For the bare CBC sample, its nanofiber surfaces and micropores contribute to the physical adsorption of polysulfides[56]. By incorporating ZIF-8 derived nitrogen-doped nanocage in NC@CBC composites, more polysulfides are absorbed due to its increased porous structure as well as the chemical binding effect after N-doing[57]. However, only the solution with FeSA-NC@CBC became almost colorless, indicating the presence of Fe SACs provided a more intense interaction with soluble LiPSs. The polysulfide adsorption ability is quantitively compared by the UV-Vis absorbance spectroscopy of the Li_2S_6 electrolyte after soaking. As depicted in **Fig. S10**, the most notable decline in UV absorbance peak intensity was observed with FeSA-NC@CBC, reaffirming its superior polysulfide adsorption capabilities. NC@CBC and CBC also exhibited polysulfide adsorption, albeit to a lesser degree, consistent with the outcomes of visual observation tests. The chemical status and interaction between the FeSA-NC@CBC and

polysulfides were further studied by XPS analysis before and after Li_2S_6 adsorption tests. As shown in the wide XPS surveys (**Fig. 3b**), new peaks appeared at 56.5 eV and 168.1 eV corresponded to the Li 1s and S 2p regions after polysulfide adsorption. As shown in the high-resolution spectra of Fe 2p (**Fig. 3c**), a noticeable shift towards lower binding energy for the Fe 2p 3/2 and Fe 2p 1/2 peaks is observed when comparing FeSA-NC@CBC in its pristine state to its state after interaction with Li2S6. This shift suggests a charge transfer from Li_2S_6 to the Fe single atoms[11]. In the high resolution spectrum of the S 2p core level (**Fig. S11**), the peaks at 163.3 and 164.6 eV are attributed to the bridge sulfur (S_B^0), and the detected signals at 166.9, 168.4, and 170.5 eV can be assigned to the thiosulfate, polythionate, and sulfate, respectively [26]. The presence of thiosulfate and polythionate, commonly recognized as the catalytic intermediates in sulfur conversion, is probably the result of surface redox reactions occurring between Fe SACs and polysulfides[58].

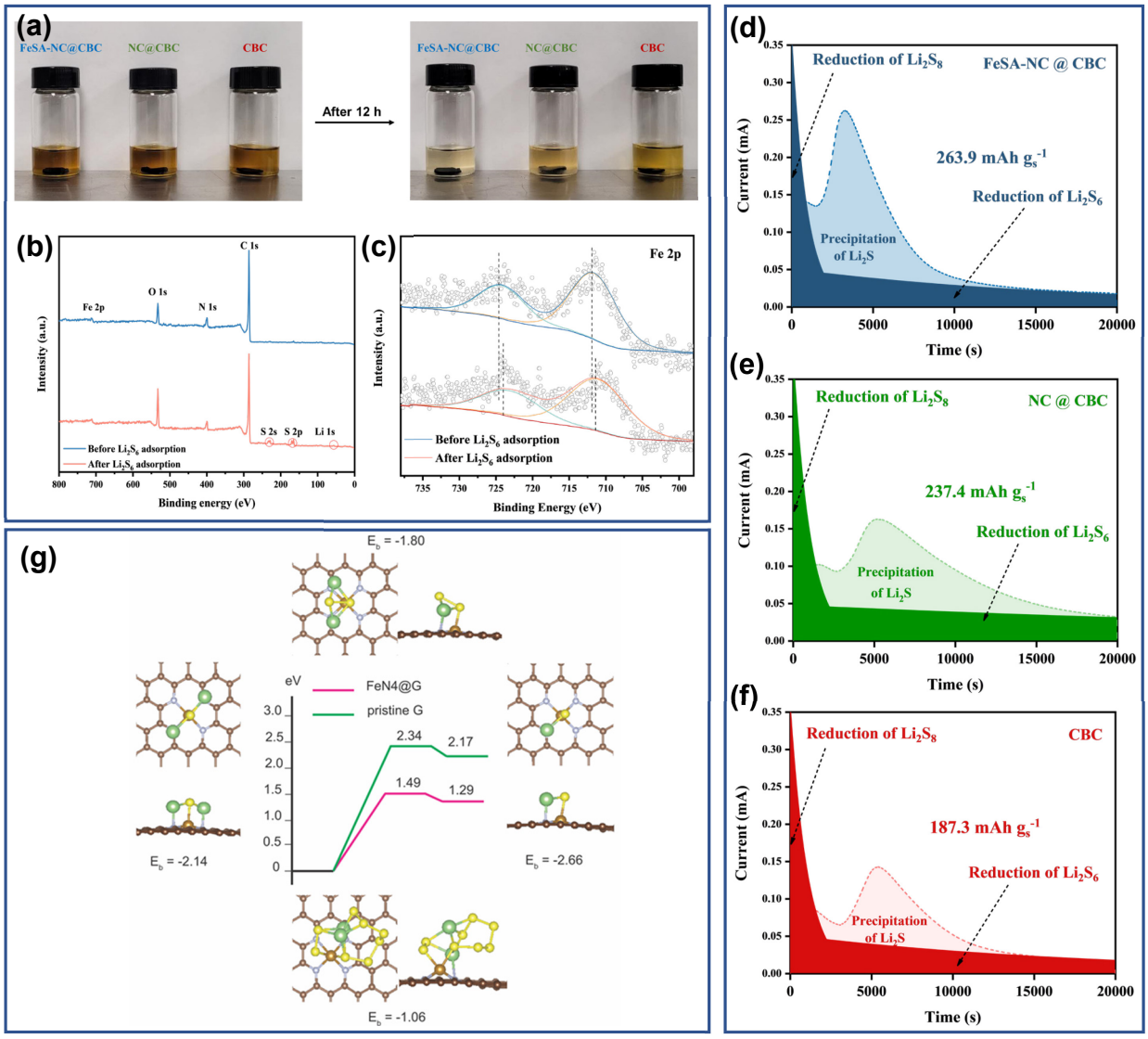

Figure 3 (a) Photos of FeSA-NC@CBC, NC@CBC and CBC initially added in 5 mM Li_2S_6 solution and after aging for 12 h. (b) XPS wide survey and (c) high-resolution Fe 2p XPS spectra of FeSA-NC@CBC before and after Li_2S_6 adsorption tests. Potentiostatic Li_2S precipitation recorded for (d)FeSA-NC@CBC, (e) NC@CBC and (f) CBC electrode. (g) The DFT-calculated adsorption energy of Li_2S and $*Li_2S_m$ (m = 1, 2, 8) on FeN_4@G and the energy barriers of activating the Li-S bond in Li_2S on FeN_4@G and pristine graphene (the units are eV).

We measured the potentiostatic Li_2S precipitation dynamics using Li-S cells with Li_2S_6 electrolyte to investigate the catalytic effect of Fe SAC in promoting Li_2S nucleation and precipitation. Three Li-S cells

with FeSA-NC@CBC, NC@CBC, and CBC-based sulfur cathodes were comparatively tested. First, we applied the potentiostatic intermittent titration technique (PITT) to probe the quasi-equilibrium potential of polysulfide to Li_2S in the typical DOL/DME electrolyte, which was found to be 2.12 V (**Fig. S12**). The three Li-S cells with Li_2S_6 electrolyte were then galvanostatically discharged to 2.12 V, followed by potentiostatically discharged at 2.11 V until the current reached 10^{-5} mA. As observed in **Fig. 3(d)-(f)**, the cell current initially dropped monotonically. This current came from charging non-faradic double layers and reducing higher order polysulfides (Li_2S_6). It monotonically decreased with diminished higher order polysulfides and completion of charging the electrical double layers. Subsequently, the cell current rose, reached a maximum, and then reduced to a background value, corresponding to the nucleation activity of solid Li_2S, followed by the growth of nucleates to form a compact insulating film, where the reaction stopped[57, 59]. FeSA-NC@CBC gave a sharp and fastest current response with the highest current (0.261 mA) and capacity (243.2 mAh g^{-1}) for Li_2S precipitation, compared to NC@CBC (0.165 mA, 208.7 mAh g^{-1}) and bare CBC electrode (0.153 mA, 187.3 mAh g^{-1}). These results indicate that the FeSA-NC@CBC exhibits the best capability to accelerate the polysulfides conversion (i.e., the Li_2S precipitation) and promote the efficient utilization of lithium polysulfides. The experimentally observed redox chemistry promotion over the well-dispersed Fe metal centers can be explained by the DFT calculation.

To evaluate the LiPS encapsulated ability of FeSA-NC and its electrocatalytic activity in the redox chemistry, DFT calculations were performed here to investigate the structure of FeN_4 embedded into graphene (FeN_4@G). **Fig. 3(g)** shows that FeN_4@G exhibits strong binding for LiS and Li_2S_m (m=1, 2, 8); the adsorption energies of LiS, Li_2S and Li_2S_2 are more negative than their binding energy with electrolyte molecules (**Fig. S13**), which reduces the shuttle effect of the lithium polysulfide. The results indicate the FeN_4@G can effectively trap the LiPS. To reach a high reversible capacity and a long-term cycling of Li-S batteries, the catalyst should also promote the redox reaction of LiPS to form Li_2S during discharging and reduce Li_2S during charging, by activating the Li-S bonds to accommodate or release Li at the electrode surface. From experimental results, FeSA-NC shows significantly higher catalytic activity compared to bare CBC. Herein, we calculate the energy barriers for activating the Li-S bond in Li_2S (transformation

between *Li_2S and *LiS +*Li) and compare the electrocatalytic performance on FeN_4@G and pristine graphene. **Fig. 3(e)** shows that FeN_4@G significantly decreases the activation barrier of this reversible reaction; the energy of the transition state over the FeN_4@G is lower than that on pristine graphene by 0.84 eV. The DFT-calculated atomic structures of initial, transition, and final states of the reaction are shown in **Fig.S14**. Initially, Li_2S adsorbs on the center active site. Following that, the Li-S bond is activated and dissociated, and the Li adatom diffuses on the substrate surface. The single-Fe center stabilizes the reaction intermediates, thereby reducing the reaction energy and consequently lowering the activation barrier for activating the Li-S bonds. During the charging the battery, such a facile dissociation of the Li-S bond facilitates lithium release from the electrode and dissolution into the electrolyte; during discharging, the activated Li-S bonds help accumulate more lithium into the polysulfides.[26, 33, 45] This result thus provides an explanation for the experimental observation of promoted redox chemistry over the well-dispersed metal centers.

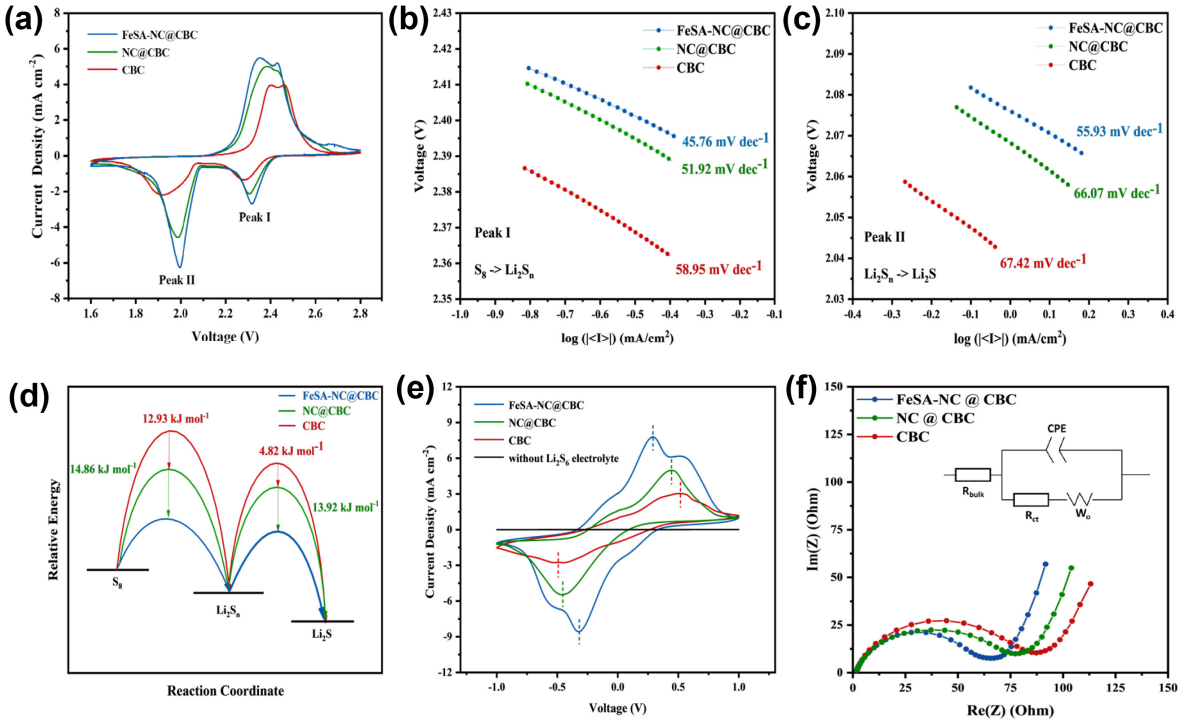

Figure 4 (a) CV profiles of the full cells assembled with FeSA-NC@CBC, NC@CBC and CBC cathodes and lithium anode at the same scan rate of 0.2 mV s^{-1}; Tafel plots of the first (b) and second (c) cathodic peaks and (d) the activation energies (Ea) of the discharge process. (e) CV profiles of Li_2S_6 symmetric cells at a 10 mV s^{-1} scan rate and (f)EIS curves for three electrodes.

Fig. 4(a) presents the CV profiles of Li-S cells with FeSA-NC@CBC, NC@CBC and CBC-based sulfur cathodes. The two cathodic peaks (Peak I and Peak II) correspond to the transformation from S_8 to Li_2S_n ($6 \leq n \leq 8$) and from Li_2S_n ($2 \leq n \leq 4$) to Li_2S, respectively. Compared to NC@CBC and bare CBC, the cell with Fe SACs exhibits higher current densities and lower potential differences between anodic and cathodic peaks, indicating that Fe SACs in the cathode decrease polarization and enhance the redox reaction of lithium polysulfides. The Tafel plots were derived from Peak I and Peak II in the CV curves. For the transition from S_8 to Li_2S_n shown in **Fig. 4(b)**, the fitted Tafel slopes are 45.76, 51.92, and 58.95 mV dec^{-1} for the FeSA-NC@CBC, NC@CBC and CBC, respectively. For the conversion reaction from short-chain Li_2S_n to Li_2S (**Fig. 4(c)**), the slopes are 55.93, 66.07, and 67.42 mV dec^{-1}, respectively. The lowest slopes

for the FeSA-NC@CBC cathode indicate the fastest redox conversions[60]. The activation energy of the discharging process was calculated using the equation[61, 62] of $E_a = E_a^0 - \frac{RT}{b}\varphi_{Red,IR}$, where b is the Tafel slopes and $\varphi_{Red,IR}$ is the irreversible potential obtained from CV profiles (see details in Supplementary Note 1). The relative activation energy for each reaction step was calculated based on the Tafel plot and displayed in **Fig. 4(d)**. The E_a values of both steps are dramatically reduced when Fe SACs were incorporated in the cathode, where the E_a differences between the FeSA-NC@CBC and NC@CBC electrodes are 14.96 kJ mol^{-1} and 13.92 kJ mol^{-1} for the reactions from S_8 to Li_2S_n (Ea_1) and from Li_2S_n to Li_2S (Ea_2). These results reveal that the Fe SACs facilitate the sulfur reduction conversion by lowering their activation energies.

The electrocatalytic effect was investigated by Li_2S_6 symmetric cells CV measurement shown in **Fig. 4(e)** containing three type of electrodes and Li_2S_6 solutions as electrolytes. The smallest potential difference between the reduction and oxidation peaks and the highest peak current intensities indicated the presence of Fe SACs in the electrodes significantly enhanced redox kinetics of lithium polysulfides conversion reactions[63]. Charge transfer resistance is an important indicator for the charge (i.e., electrons and lithium ions) transportation. The electrochemical impedance spectroscopy (EIS) results of fresh assembled cells were plotted in **Fig. 4(f)**. All the EIS spectra consist of a semicircle and an inclined line[64], which can be fitted by the equivalent circuit model. The R_{bulk} represents the bulk internal resistance of the electrolyte, separator and electron interfaces. R_{ct} is the charge transfer resistance. W_o is the Warburg diffusion and CPE means a constant phase element. As presented in **Fig. 4(f)**, FeSA-NC@CBC has the smallest semicircle diameter in the high-frequency range, which indicates the lowest charge transfer resistance and fastest reduction reaction kinetics within the cathode. The linear part at low frequencies represents the ion diffusion process within the cathode.

We further evaluated the charge-transport characteristics by conducting CV measurements of the Li-S battery cells under different scan rates from 0.1 to 0.5 mV s^{-1}, which are displayed in **Fig. S15(a)-(c)**. A distinguishable positive shift in cathode anodic peaks and negative shift in cathodic peaks can be observed with the increasing scan

rate, leading to an increasing polarization voltage at higher rates. For each redox peak, a linear relationship between the peak current density I_p and square root of scan rate $v^{1/2}$ was extracted, which can be fitted using the equation $I_P = 2.69 \times 10^5 n^{3/2} A D^{1/2} v^{1/2} C_{Li}$, where n, A, and C_{Li} represent the charge transfer number, the active electrode geometric area, and the concentration of Li^+ in the cathode, respectively[65]. The slope comparison of the linear fitting ($I_p/v^{0.5}$) can determine the difference of the lithium-ion diffusion rate D_{Li^+} in three different electrodes since n, A, and C_{Li} are unchanged. As presented in **Fig. S15(d)-(f)**, FeSA-NC@CBC exhibits highest slopes at each redox peak which represents the fastest lithium-ion diffusion and facilitates the sulfur transformation chemistry. D_{Li^+} also corresponds to LiPSs adsorption and Li_2S catalyzing conversion capability, since it can reflect the viscosity of LiPSs in electrolyte, or deposition of a thick Li_2S insulating layer on the electrode[66].

LSB performance test

Fig. 5 (a)-(d) displayed the charge-discharge curves and compared the rate capability of each composite cathode. Benefiting from the advantageous electrochemical kinetics, FeSA-NC@CBC-based sulfur cathode exhibited excellent rate performance delivering reversible capacities of 1338, 1215, 1104, 1030, 975 and 840 mAh g^{-1} at a rate of 0.1, 0.2, 0.3, 0.5, 1 and 2C, respectively. When the charge–discharge rate cycles shift back to 0.5 C from high rates, the cell recovered a specific capacity of 1009 mAh/g. The conspicuous two-step discharge plateau is still observed at a high rate of 2C. In contrast, the capacity rapidly declined for both NC@CBC/S (633 mAh g^{-1}) and CBC/S cathodes (367 mAh g^{-1}) when the current density increased to 2C, and the second discharge plateau nearly vanished at 2C for CBC/S cathode. Based on the charge/discharge profiles of three different electrodes recorded at 0.1C (**Fig. S16(a)**), the FeSA-NC@CBC/S exhibits the slightest polarization ($\Delta E = 152.7$ mV) as compared to those of NC@CBC/S and CBC/S, indicating better sulfur redox kinetics. As shown in **Fig. 5(e)**, positive overpotential peaks are observed at the beginning of the first charge plateaus, from which the energy barrier for converting solid Li_2S to soluble LiPSs can be evaluated[30]. Similarly, at the second discharge plateaus presented in **Fig. S16(b)**, the negative overpotential peaks can be utilized to assess the activation energy barrier for converting soluble Li_2S_4 to solid Li_2S_2. It is observed that the FeSA-NC@CBC/S electrode features the lowest overpotentials in

both the discharge and charge profiles, which is consistent with the previous electrochemical tests and indicates improved electrochemical kinetics of LiPSs on FeSA-NC@CBC electrodes.

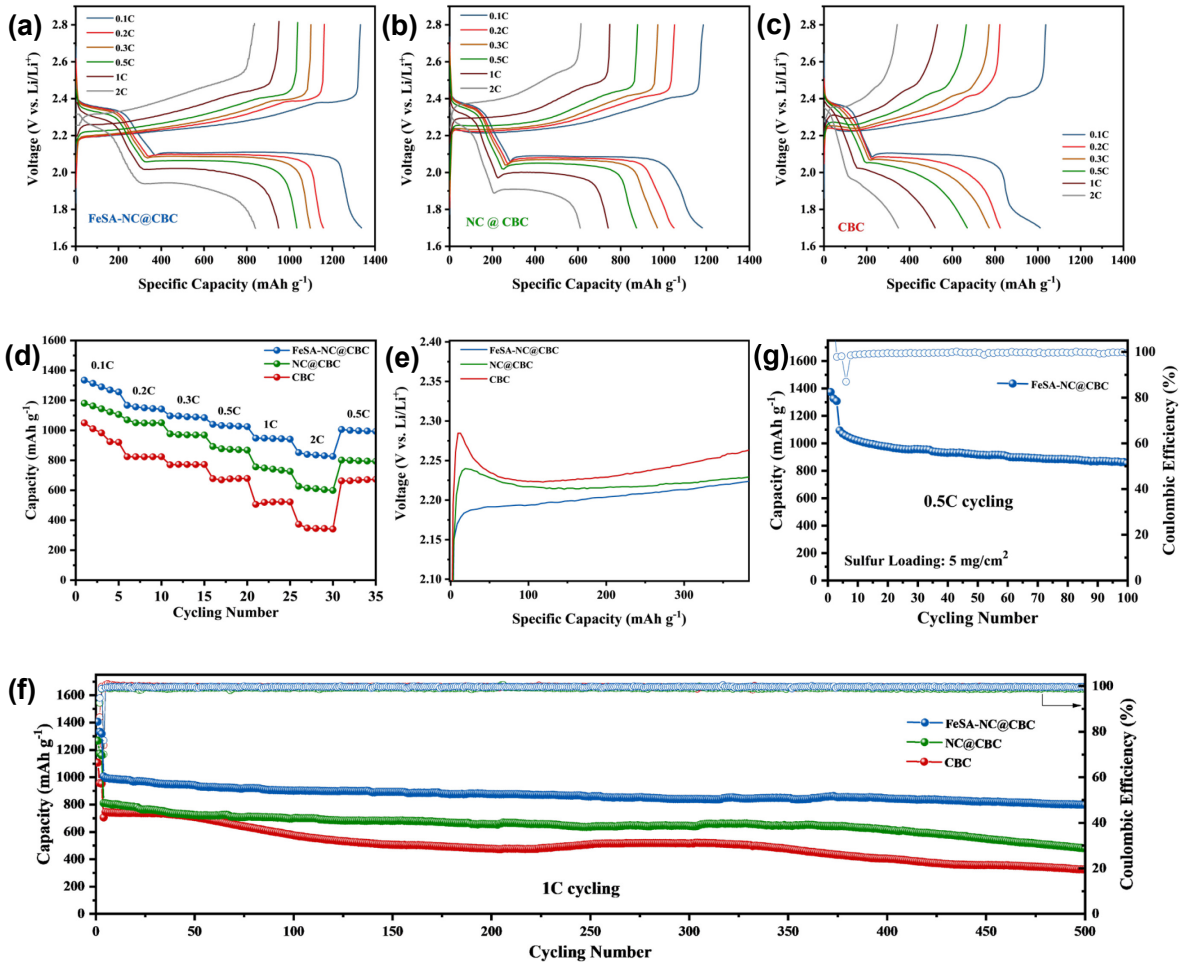

Figure 5 Galvanostatic charge and discharge curves of (a) FeSA-NC@CBC, (b) NC@CBC and (c) CBC electrodes. (d) Rate performance from 0.1 to 2 C of three types of electrodes. (e) Charge profiles of FeSA-NC@CBC, NC@CBC and CBC electrodes showing the overpotentials of polysulfide conversion reaction. (f) 1C long-term cycling performance comparison among three composite cathodes. (g) Cycling test of FeSA-NC@CBC based cell with 5 mg/cm^2 high S loading.

The 1C cycling performance is presented in **Fig. 5(f)**, further demonstrating the superiority of the FeSA-NC@CBC/S cathode. After three formation cycles at 0.05 C, the initial specific capacities of the cathodes at 1C were

1006.2, 810.3 and 705.8 mAh g^{-1} for FeSA-NC@CBC, NC@CBC, and CBC-based electrodes, respectively. After 500 cycles, the capacity of FeSA-NC@CBC remained at 799.8 mAh/g, with the Coulomb Efficiency above 98.7%. In contrast, for NC@CBC/S and CBC/S cathodes, the capacities were only retained at 481.3 and 327.1 mAh/g after 500 cycles at 1C. The measured capacity decay of FeSA-NC@CBC/S cathode is indeed low, with a 0.042% degradation rate per cycle at 1C. These different performances between FeSA-NC@CBC and NC@CBC-based cathodes again validate that Fe SAC can accelerate polysulfide conversion and improve the electrochemical performance of Li-S batteries. The enhanced performance by NC@CBC over bare CBC is attributed to the introduction of carbonized N-doped nanocages into the cathode structure. The carbonized N-doped nanocages (NC) possess abundant micropores and N-heteroatom dopants, which can better suppress the shuttle effect through physical adsorption and chemical binding. To achieve the practical goal of Li-S batteries, a composite cathode with higher sulfur loading was obtained by adding appropriate amounts of Li_2S_6 catholyte. As shown in **Fig. 5(g)**, when the S loading is increased to 5 mg/cm^2, after being activated at 0.05C for 3 cycles, the FeSA-NC@CBC based composite cathode still possesses an outstanding cyclic stability at 0.5 C with a high capacity of 861 mAh g^{-1} after 100 cycles.

The sulfur contents of the FeSA-NC@CBC/S composites with sulfur loading of 2.5 and 5 mg cm^{-2} were determined to be 72.4 and 81.2 wt%, respectively, through the TGA curves shown in **Fig. S17**. The freestanding structure coupled with polysulfide catholyte enables the fabrication of sulfur-electrode with tunable sulfur loading and content. The FeSA-NC@CBC sample loaded with polysulfide catholyte was first fully charged to ensure the active material was totally converted to solid sulfur. Lithium nitrite is commonly employed in Li-S systems, which is believed to passivate metallic lithium and suppress polysulfide shuttle effect [67]. Therefore, we also tested the electrochemical performances of FeSA-NC@CBC based cathode with a sulfur loading of 5 mg cm^{-2} in the electrolyte without $LiNO_3$. As shown in **Fig. S18**, the Coulombic efficiency of the FeSA-NC@CBC/S slightly declined from 99.03% to 96.32% in the electrolyte without $LiNO_3$, which confirms the significance of $LiNO_3$ to reduce active materials degradation. However, the Li-S cells coupled with FeSA-NC@CBC/S still possess a stable cycling performance with a specific capacity of 668 mAh g^{-1} after 100 cycles at 0.5 C, indicating the capture and conversion effect of FeSACs to reduce the dissolved LiPSs in the electrolyte. A lower E/S ratio is desired for

achieving practical Li-S batteries with higher energy density. As shown in **Fig. S19**, FeSA-NC@CBC with a high sulfur loading of 5 mg cm^{-2} and an E/S ratio of 7.5 ul mg^{-1} retained a capacity of 705 mAh g^{-1} after cycling at 0.3 C for 100 cycles. Prior to cycling under low E/S ratio condition, the assembled cell was first activated at 0.05C for 5 cycles to allow sufficient electrolyte infiltration.

The excellent rate capability and cycling stability of FeSA-NC@CBC-based Li-S battery cells are a direct result of accelerated polysulfide redox kinetics, catalyzed by FeSA-NC under the assistance of CBC: 1) the highly conductive interconnected 3D framework of CBC enables fast electron and Li^+ transportation and buffer volume expansion, 2) the nanoporous structure of FeSA-NC physically confines soluble LiPS, while the polar Fe-N_4 moieties provide strong chemical binding to trap LiPS, and 3) the facile sulfides redox reaction kinetics efficiently accelerated by atomically dispersed FeSA catalysts. In **Table 1**, we compare our LSB performances with several representative works that applied SACs in Li-S batteries.

Table 1. Comparison of the electrochemical performance of LSBs using different single atom catalytic materials.

SACs materials	Sulfur loading (mg/cm^2)	Rate capability (mAh/g)	Cycling performance (mAh/g)	Ref.
FeSA-NC@CBC	2.5	840 at 2C	799.8 (500th) at 1C	This work
FeSA-NC@CBC	5	-	861 (100th) at 0.5C	This work
FeNSC	1.0	550 at 4C	477 (1000th) at 1C	[68]
Fe-N_5-C	1.0	723 at 3C	662 (500th) at 1C	[69]
Ni-MOS_2@PP	2.5	677 at 3C	868 (100th) at 0.5C	[31]
Ni-N_5/HNPC	1.3-1.6	684 at 4C	798 (500th) at 0.5C	[70]
SA-Co/NGM@PP	1.5	649 at 5C	731 (1000th) at 2C	[32]
SACo@NG	2.0	~550 at 3C	513(400th) at 0.5C	[45]
SAV@NG	2.0	645 at 3C	551 (400th) at 0.5C	[45]

Conclusion

A freestanding structure of Fe single atom catalyst functionalized N-doped carbon nanocages linked by a carbon nanofiber network (FeSA-NC@CBC) was fabricated, which was applied as a scaffold to fabricate sulfur cathodes used in Li-S batteries. Material characterizations indicated formation of Fe single atoms coordinated with N-dopants in carbon. Electrochemical studies revealed Fe single atom catalytic functions in the discharge process including lowering energy barriers for S_8 reduction to liquid-phase LiPSs and further to solid-phase Li_2S_2/Li_2S and accelerating Li_2S_2/Li_2S nucleation and deposition, as well as its catalytic functions in the charge process. The experimental observations were further corroborated by our DFT-based theoretical calculation results. The improved sulfide reaction kinetics diminishes LiPS shuttle effects and therefore improves LBS rate performance and cycling stability, confirmed by our battery test results. The fabricated FeSA-NC@CBC/S composite cathode with a sulfur loading of 2.5 mg cm^{-2} and sulfur content of 72.4% delivered a high initial capacity of 1338 mA h g^{-1} at 0.1 C, and a slow capacity decay rate of 0.042 % per cycle up to 500 cycles at 1 C during cycling test.

Experimental Section

Material synthesis

Synthesis of Fe-ZIF-8 powder and Fe-ZIF-8@BC aerogel: A purified BC pellicle (3.5 × 5 × 0.5 cm), 1.07 g $Zn(NO_3)_2 \cdot 6H_2O$, and 0.127 g $Fe(acac)_3$ were dispersed in 50 mL methanol solution and stirred for 12 h. Another 50 ml methanol solution dissolved with 2.36 g 2-methylimidazole (MI) was also prepared. Two methanolic solutions were then mixed and ultrasonicated for 1 h. The obtained mixture was loaded into a 100 ml Teflon-lined stainless-steel autoclave for heat treatment at 120 °C for 4 h. The obtained yellowish gel was then rinsed with methanol and DI water several times and freeze-dried for 48 h to prepare the Fe-ZIF-8@BC composite aerogel. ZIF-8@BC aerogel was prepared by the same procedure without adding $Fe(acac)_3$ salt. Pure Fe-ZIF-8 powder without mixing with BC was synthesized in a similar procedure. By varying the molar ratio between metal salts and MI, Fe-ZIF-8 particle size can be tuned.

Fabrication of FeSA-NC@CBC sulfur host: The Fe-ZIF-8@BC aerogel was transferred into a tube furnace and carbonized at 900 ℃ for 3 h with a heating rate of 5 ℃/min under an Ar atmosphere to obtain the FeSA-NC@CBC sulfur host. The same carbonization process was used to prepare NC@CBC and CBC electrode hosts from ZIF-8@BC and blank BC aerogels, respectively. The obtained freestanding electrode hosts were punched into 12 mm disks for coin cell assembling. Pure FeSA-NC powder was also prepared by direct pyrolysis of Fe-ZIF-8 powder for material characterization.

Material characterization

The morphologies and architectures of the prepared samples were observed by scanning electron microscopy at 5kV (SEM, Zeiss Auriga). The porous microstructures were characterized by a transmission electron microscopy at 200kV (TEM, JEOL 2010F). Aberration-corrected high-angle annular dark-field scanning transmission electron microscopy (AC-HAADF-STEM) was performed on Nion UltraSTEM 100 at 60 kV. Annular dark-field scanning transmission electron microscopy (ADF-STEM) and the energy dispersive X-ray spectra (EDX) elemental mapping were recorded on JEOL ARM200F at 200kV. X-ray absorption near-edge structure (XANES) and the extended X-ray absorption fine structure (EXAFS) for Fe K-edge were performed at beamline 7-BM, NSLS-II, Brookhaven National Laboratory. X-ray photon energy was monochromatized by an Si(111) channel-cut crystal monochromator running in continuous scan mode. Higher-order harmonic contaminations were eliminated by detuning the monochromator to reduce the incident X-ray intensity by approximately 30%. All spectra were collected at room temperature in the fluorescence mode. The Brunauer-Emmett-Teller (BET) measurement was performed to obtain the specific surface area and pore size distribution using a porosity analyzer (Tristar II Plus). The crystalline structure was recorded by X-ray diffraction (XRD) with Cu Kα radiation ($\lambda = 0.1541$ nm) on an X-ray Diffractometer (Malvern PANalytical Aeris). The X-ray photoelectron spectroscopy (XPS) study was conducted on a spectrometer (Krator Axis Supra + apparatus) using Al K-alpha (1486.6 eV) as the excitation light source. UV-Vis Spectrometer (Perkin Lambda 950) was used to acquire UV-vis absorbance spectroscopy after

polysulfide adsorption tests. Thermogravimetric analysis (TGA, LABSYS EVO) was performed under helium atmosphere with a heating rate of 5 °C min^{-1}.

Electrochemical measurements

A 0.25 M Li_2S_6 solution was prepared by mixing stoichiometric amounts of sublimed sulfur and Li_2S in a molar ratio of 1:5 in 1,2-dimethoxyeethane (DME) and 1,3-dioxolane (DOL) solvent (1:1, v/v) under stirring at 60 °C until the sulfur was fully dissolved, which finally formed a brown solution. To prepare the ether-based electrolyte, 1.0 M lithium bis(trifluoromethanesulfonyl)imide (LiTFSI) was dissolved in DME/DOL in a 1:1 volumetric ratio with 2 wt.% lithium nitrides ($LiNO_3$) as an additive.

Visual lithium polysulfide adsorption test: The 0.25 M Li_2S_6 solution was diluted to 0.05 M for the visual adsorption test. FeSA-NC@CBC, NC@CBC and CBC samples with an area of 1.13 cm^{-2} were loaded into 4 mL 0.05 M Li_2S_6 solution separately to observe the color evolution. All samples were vacuum-dried at 80 °C overnight before testing.

Assembly of Li_2S_6 symmetric cells and cyclic voltammogram (CV) measurement: The Li_2S_6 symmetric cells were assembled using identical electrodes loaded with 20 μL Li_2S_6 (0.25 M) electrolyte serving as working and counter electrodes. The Li_2S_6 symmetric cells CV measurements were carried out at a scan rate of 30 mV s^{-1} with a potential window between −1 and 1 V to evaluate the polysulfide conversion kinetics.

Li_2S precipitation test: 0.25 M Li_2S_8 was prepared by mixing S and Li_2S in a molar ratio of 7:1 in a blank electrolyte. Then 20 μL Li_2S_8 (0.25 M) catholyte was dropped on each freestanding electrode and another 20 μL blank electrolyte was added on the Li anode, respectively. The assembled cell was first galvanostatically discharged with a constant current (0.112 mA) to 2.12 V and then potentiostatically held at 2.11 V until the current decreased to 1×10^{-5} mA[57].

Li-S coin cell battery assembly and electrochemical performance test: 60 μL 0.25 M Li_2S_6 catholyte was dropped on the FeSA-NC@CBC, NC@CBC, and CBC freestanding hosts to obtain the composite cathodes with a sulfur loading of 2.5 mg cm^{-2}. For the FeSA-NC@CBC based composite cathode with a

512 diameter of 12 mm, the mass of FeSA-NC@CBC itself is ~ 1.1 mg, and the S content is determined to be
513 72.4% by TGA. A high sulfur loading FeSA-NC@CBC based cathode was also prepared with a sulfur
514 loading of 5 mg cm^{-2} and the corresponding S content is 81.4%. CR 2016-type coin cells were assembled
515 in an argon-filled glove box using the prepared composite cathodes, Celgard 2400 membranes as the
516 separators, and 0.6 mm thick lithium chip as the anode. The CV for the assembled full cells were tested
517 from 1.6 to 2.8 V at a scan rate from 0.1 to 0.5 mV s^{-1} and the electrochemical impedance spectrum (EIS)
518 was tested in the range of 100 kHz–0.01 Hz with an AC voltage amplitude of 5 mV. The CV and EIS
519 measurements were performed on a Biologic SP-240 electrochemical workstation. The galvanostatic
520 charge–discharge curves of these Li-S cells were recorded on a LANDCT2001A battery tester under
521 different current rates within a voltage range of 1.7 - 2.8 V. The E/S ratio used for typical electrochemical
522 tests was 15 ul/mg. A low E/S ratio of 7.5 ul/mg was used in the 0.3 C cyclability test with a sulfur loading
523 of 5 mg cm^{-2}.
524
525 **Computational methods**
526 All spin-polarized periodic density functional theory (DFT) calculations in this work were employed
527 using the Vienna *ab initio* simulation package (VASP)[71]. To describe the exchange-correlation
528 interaction, a generalized gradient approximation (GGA) in the form of Perdew-Burke-Ernzerhof (PBE)
529 functional was applied here[72], with the DFT-D3 method to account for the van der Waals interaction[73].
530 The projector augmented wave (PAW) method was adopted to treat the ion-electron interaction[74, 75].
531 The Brillouin zone was sampled with a single k point for geometric optimization. All energy values were
532 calculated with constant charge and without applying additional electrode potential. A 20 Å vacuum along
533 z-direction was utilized to minimize the interaction between adjacent cells. The supercell was modeled as
534 a pristine graphene slab containing 160 C atoms, which was used in our previous work[40, 76, 77]. The
535 periodic system was constructed by removing two neighboring C atoms to create a divacancy followed by
536 N substitution and Fe incorporation. The activation barriers were calculated by using the climbing-image

nudged elastic band (NEB) method[78]. The transition states were further confirmed by single imaginary frequency in vibrational analyses.

Acknowledgements

This work is supported by the National Science Foundation under Grants 2129983, 2129982, and 2103582. The computational simulations were performed at the OU Supercomputing Center for Education & Research. We acknowledge the use of facilities within the Eyring Materials Center at Arizona State University supported in part by NNCI-ECCS-1542160. This research used resources 7-BM of the National Synchrotron Light Source II, a U.S. Department of Energy (DOE) Office of Science User Facility operated for the DOE Office of Science by Brookhaven National Laboratory under Contract No. DE-SC0012704.

Reference

[1] X. Ji, L.F. Nazar, Advances in Li–S batteries, Journal of Materials Chemistry 20(44) (2010) 9821-9826.
[2] J. Zheng, J. Tian, D. Wu, M. Gu, W. Xu, C. Wang, F. Gao, M.H. Engelhard, J.-G. Zhang, J. Liu, J. Xiao, Lewis Acid–Base Interactions between Polysulfides and Metal Organic Framework in Lithium Sulfur Batteries, Nano Letters 14(5) (2014) 2345-2352.
[3] A. Rosenman, E. Markevich, G. Salitra, D. Aurbach, A. Garsuch, F.F. Chesneau, Review on Li‐sulfur battery systems: An integral perspective, Advanced Energy Materials 5(16) (2015) 1500212.
[4] J. He, A. Bhargav, A. Manthiram, Covalent Organic Framework as an Efficient Protection Layer for a Stable Lithium-Metal Anode, Angewandte Chemie International Edition 61(18) (2022) e202116586.
[5] B. Yu, D. Chen, Z. Wang, F. Qi, X. Zhang, X. Wang, Y. Hu, B. Wang, W. Zhang, Y. Chen, J. He, W. He, Mo2C quantum dots@graphene functionalized separator toward high-current-density lithium metal anodes for ultrastable Li-S batteries, Chemical Engineering Journal 399 (2020) 125837.
[6] M.R. Busche, P. Adelhelm, H. Sommer, H. Schneider, K. Leitner, J. Janek, Systematical electrochemical study on the parasitic shuttle-effect in lithium-sulfur-cells at different temperatures and different rates, Journal of Power Sources 259 (2014) 289-299.
[7] G. Ren, S. Li, Z.-X. Fan, J. Warzywoda, Z. Fan, Soybean-derived hierarchical porous carbon with large sulfur loading and sulfur content for high-performance lithium–sulfur batteries, Journal of Materials Chemistry A 4(42) (2016) 16507-16515.
[8] D. Gueon, M.-Y. Ju, J.H. Moon, Complete encapsulation of sulfur through interfacial energy control of sulfur solutions for high-performance Li−S batteries, Proceedings of the National Academy of Sciences 117(23) (2020) 12686-12692.
[9] L. Ji, M. Rao, H. Zheng, L. Zhang, Y. Li, W. Duan, J. Guo, E.J. Cairns, Y. Zhang, Graphene oxide as a sulfur immobilizer in high performance lithium/sulfur cells, Journal of the American Chemical Society 133(46) (2011) 18522-18525.

[10] W. Gao, Z. Wang, C. Peng, S. Kang, L. Cui, Accelerating the redox kinetics by catalytic activation of “dead sulfur” in lithium–sulfur batteries, Journal of Materials Chemistry A 9(23) (2021) 13442-13458.
[11] W. Sun, S. Liu, Y. Li, D. Wang, Q. Guo, X. Hong, K. Xie, Z. Ma, C. Zheng, S. Xiong, Monodispersed FeS2 Electrocatalyst Anchored to Nitrogen-Doped Carbon Host for Lithium–Sulfur Batteries, Advanced Functional Materials 32(43) (2022) 2205471.
[12] W.-G. Lim, S. Kim, C. Jo, J. Lee, A Comprehensive Review of Materials with Catalytic Effects in Li–S Batteries: Enhanced Redox Kinetics, Angewandte Chemie International Edition 58(52) (2019) 18746-18757.
[13] T. Peng, N. Zhang, Y. Wang, M. Zhao, W. Sun, D. Zhang, H. Yan, Y. Lu, Y. Luo, Rooting MnO2 nanosheet on carbon nanoboxes as efficient catalytic host for lithium–sulfur battery, Journal of Solid State Electrochemistry 25(2) (2021) 505-512.
[14] T. Peng, N. Zhang, Y. Yang, M. Zhang, R. Luo, C. Chen, Y. Lu, Y. Luo, Crystal Facet Engineering of MXene-Derived TiN Nanoflakes as Efficient Bidirectional Electrocatalyst for Advanced Lithium-Sulfur Batteries, Small 18(38) (2022) 2202917.
[15] W. Sun, Y. Li, S. Liu, C. Liu, X. Tan, K. Xie, Mechanism investigation of iron selenide as polysulfide mediator for long-life lithium-sulfur batteries, Chemical Engineering Journal 416 (2021) 129166.
[16] J. Feng, C. Shi, H. Dong, C. Zhang, W. Liu, Y. Liu, T. Wang, X. Zhao, S. Chen, J. Song, Design of ZnSe-CoSe heterostructure decorated in hollow N-doped carbon nanocage with generous adsorption and catalysis sites for the reversibly fast kinetics of polysulfide conversion, Journal of Energy Chemistry 86 (2023) 135-145.
[17] J. He, A. Bhargav, A. Manthiram, Molybdenum Boride as an Efficient Catalyst for Polysulfide Redox to Enable High-Energy-Density Lithium–Sulfur Batteries, Advanced Materials 32(40) (2020) 2004741.
[18] B. Yu, A. Huang, K. Srinivas, X. Zhang, F. Ma, X. Wang, D. Chen, B. Wang, W. Zhang, Z. Wang, J. He, Y. Chen, Outstanding Catalytic Effects of 1T′ -MoTe2 Quantum Dots@3D Graphene in Shuttle-Free Li–S Batteries, ACS Nano 15(8) (2021) 13279-13288.
[19] J. He, A. Bhargav, A. Manthiram, In Situ Grown 1T′ -MoTe2 Nanosheets on Carbon Nanotubes as an Efficient Electrocatalyst and Lithium Regulator for Stable Lithium‐Sulfur Full Cells, Advanced Energy Materials 12(1) (2022) 2103204.
[20] X. Lin, W. Li, X. Pan, S. Wang, Z. Fan, Electrocatalytic and Conductive Vanadium Oxide on Carbonized Bacterial Cellulose Aerogel for the Sulfur Cathode in Li-S Batteries, Batteries 9(1) (2023) 14.
[21] C. Zhang, J. Feng, X. Guo, J. Zhang, W. Zhang, L. Zhang, J. Song, G. Shao, G. Wang, Blocking polysulfide by physical confinement and catalytic conversion of SiO2@MXene for Li–S battery, Applied Physics Letters 122(19) (2023).
[22] Y. Liu, W. Kou, X. Li, C. Huang, R. Shui, G. He, Constructing patch‐Ni‐shelled Pt@ Ni nanoparticles within confined nanoreactors for catalytic oxidation of insoluble polysulfides in Li‐S batteries, Small 15(34) (2019) 1902431.
[23] M. Hagen, D. Hanselmann, K. Ahlbrecht, R. Maça, D. Gerber, J. Tübke, Lithium‐sulfur cells: the gap between the state‐of‐the‐art and the requirements for high energy battery cells, Advanced Energy Materials 5(16) (2015) 1401986.
[24] D. Eroglu, K.R. Zavadil, K.G. Gallagher, Critical link between materials chemistry and cell-level design for high energy density and low cost lithium-sulfur transportation battery, Journal of The Electrochemical Society 162(6) (2015) A982-A990.
[25] J. Wang, L. Jia, J. Zhong, Q. Xiao, C. Wang, K. Zang, H. Liu, H. Zheng, J. Luo, J. Yang, Single-atom catalyst boosts electrochemical conversion reactions in batteries, Energy Storage Materials 18 (2019) 246-252.
[26] C. Dong, C. Zhou, M. Wu, Y. Yu, K. Yu, K. Yan, C. Shen, J. Gu, M. Yan, C. Sun, L. Mai, X. Xu, Boosting Bi-Directional Redox of Sulfur with Dual Metal Single Atom Pairs in Carbon Spheres Toward

High-Rate and Long-Cycling Lithium–Sulfur Battery, Advanced Energy Materials 13(30) (2023) 2301505.
[27] H. Liu, X. Peng, X. Liu, Single‐Atom Catalysts for the Hydrogen Evolution Reaction, ChemElectroChem 5(20) (2018) 2963-2974.
[28] J. Li, S. Chen, N. Yang, M. Deng, S. Ibraheem, J. Deng, J. Li, L. Li, Z. Wei, Ultrahigh‐loading zinc single‐atom catalyst for highly efficient oxygen reduction in both acidic and alkaline media, Angewandte Chemie International Edition 58(21) (2019) 7035-7039.
[29] Y. Li, S. Lin, D. Wang, T. Gao, J. Song, P. Zhou, Z. Xu, Z. Yang, N. Xiao, S. Guo, Single Atom Array Mimic on Ultrathin MOF Nanosheets Boosts the Safety and Life of Lithium–Sulfur Batteries, Advanced Materials 32(8) (2020) 1906722.
[30] Z. Du, X. Chen, W. Hu, C. Chuang, S. Xie, A. Hu, W. Yan, X. Kong, X. Wu, H. Ji, L.-J. Wan, Cobalt in Nitrogen-Doped Graphene as Single-Atom Catalyst for High-Sulfur Content Lithium–Sulfur Batteries, Journal of the American Chemical Society 141(9) (2019) 3977-3985.
[31] C. Dong, C. Zhou, Y. Li, Y. Yu, T. Zhao, G. Zhang, X. Chen, K. Yan, L. Mai, X. Xu, Ni Single Atoms on MoS2 Nanosheets Enabling Enhanced Kinetics of Li-S Batteries, Small 19(4) (2023) 2205855.
[32] D. Wang, K. Ma, J. Hao, W. Zhang, H. Shi, C. Wang, Z. Xiong, Z. Bai, F.-R. Chen, J. Guo, B. Xu, X. Yan, Y. Gu, Engineering single-atom catalysts as multifunctional polysulfide and lithium regulators toward kinetically accelerated and durable lithium-sulfur batteries, Chemical Engineering Journal 466 (2023) 143182.
[33] Z. Han, S. Zhao, J. Xiao, X. Zhong, J. Sheng, W. Lv, Q. Zhang, G. Zhou, H.-M. Cheng, Engineering d-p Orbital Hybridization in Single-Atom Metal-Embedded Three-Dimensional Electrodes for Li–S Batteries, Advanced Materials 33(44) (2021) 2105947.
[34] A. Han, B. Wang, A. Kumar, Y. Qin, J. Jin, X. Wang, C. Yang, B. Dong, Y. Jia, J. Liu, Recent advances for MOF‐derived carbon‐supported single‐atom catalysts, Small Methods 3(9) (2019) 1800471.
[35] Y. Chen, S. Ji, Y. Wang, J. Dong, W. Chen, Z. Li, R. Shen, L. Zheng, Z. Zhuang, D. Wang, Isolated single iron atoms anchored on N‐doped porous carbon as an efficient electrocatalyst for the oxygen reduction reaction, Angewandte Chemie 129(24) (2017) 7041-7045.
[36] C. Zhou, Z. Li, X. Xu, L. Mai, Metal-organic frameworks enable broad strategies for lithium-sulfur batteries, National Science Review 8(12) (2021).
[37] J. Li, J. Zhou, T. Wang, X. Chen, Y. Zhang, Q. Wan, J. Zhu, Covalent sulfur embedding in inherent N,P co-doped biological carbon for ultrastable and high rate lithium–sulfur batteries, Nanoscale 12(16) (2020) 8991-8996.
[38] H. Bian, J. Luo, R. Wang, X. Zhou, S. Ni, R. Shi, G. Fang, H. Dai, Recyclable and reusable maleic acid for efficient production of cellulose nanofibrils with stable performance, ACS Sustainable Chemistry Engineering 7(24) (2019) 20022-20031.
[39] W. Lei, D. Jin, H. Liu, Z. Tong, H. Zhang, An overview of bacterial cellulose in flexible electrochemical energy storage, ChemSusChem 13(15) (2020) 3731-3753.
[40] S. Li, J. Warzywoda, S. Wang, G. Ren, Z. Fan, Bacterial cellulose derived carbon nanofiber aerogel with lithium polysulfide catholyte for lithium–sulfur batteries, Carbon 124 (2017) 212-218.
[41] Y. Huang, K. Tang, F. Yuan, W. Zhang, B. Li, F. Seidi, H. Xiao, D. Sun, N-doped porous carbon nanofibers fabricated by bacterial cellulose-directed templating growth of MOF crystals for efficient oxygen reduction reaction and sodium-ion storage, Carbon 168 (2020) 12-21.
[42] R. Xiao, K. Chen, X. Zhang, Z. Yang, G. Hu, Z. Sun, H.-M. Cheng, F. Li, Single-atom catalysts for metal-sulfur batteries: Current progress and future perspectives, Journal of Energy Chemistry 54 (2021) 452-466.
[43] Y. Huang, M. Zheng, Z. Lin, B. Zhao, S. Zhang, J. Yang, C. Zhu, H. Zhang, D. Sun, Y. Shi, Flexible cathodes and multifunctional interlayers based on carbonized bacterial cellulose for high-performance lithium–sulfur batteries, Journal of Materials Chemistry A 3(20) (2015) 10910-10918.

[44] Y. Cheng, S. Zhao, B. Johannessen, J.P. Veder, M. Saunders, M.R. Rowles, M. Cheng, C. Liu, M.F. Chisholm, R. De Marco, Atomically dispersed transition metals on carbon nanotubes with ultrahigh loading for selective electrochemical carbon dioxide reduction, Advanced Materials 30(13) (2018) 1706287.
[45] G. Zhou, S. Zhao, T. Wang, S.-Z. Yang, B. Johannessen, H. Chen, C. Liu, Y. Ye, Y. Wu, Y. Peng, C. Liu, S.P. Jiang, Q. Zhang, Y. Cui, Theoretical Calculation Guided Design of Single-Atom Catalysts toward Fast Kinetic and Long-Life Li–S Batteries, Nano Letters 20(2) (2020) 1252-1261.
[46] Y. Cheng, S. He, S. Lu, J.P. Veder, B. Johannessen, L. Thomsen, M. Saunders, T. Becker, R. De Marco, Q. Li, Iron single atoms on graphene as nonprecious metal catalysts for high‐temperature polymer electrolyte membrane fuel cells, Advanced science 6(10) (2019) 1802066.
[47] X. Wan, X. Liu, Y. Li, R. Yu, L. Zheng, W. Yan, H. Wang, M. Xu, J. Shui, Fe–N–C electrocatalyst with dense active sites and efficient mass transport for high-performance proton exchange membrane fuel cells, Nature Catalysis 2(3) (2019) 259-268.
[48] Y. Pan, Y. Chen, K. Wu, Z. Chen, S. Liu, X. Cao, W.-C. Cheong, T. Meng, J. Luo, L. Zheng, C. Liu, D. Wang, Q. Peng, J. Li, C. Chen, Regulating the coordination structure of single-atom Fe-NxCy catalytic sites for benzene oxidation, Nature Communications 10(1) (2019) 4290.
[49] J. Wang, C.-X. Zhao, J.-N. Liu, D. Ren, X. Ma, B.-Q. Li, J.-Q. Huang, Q. Zhang, Composing atomic transition metal sites for high-performance bifunctional oxygen electrocatalysis in rechargeable zinc–air batteries, Particuology (2022).
[50] Y. Ma, D. Chen, D. Zhang, H. Yu, Y. Zheng, W. Li, L. Wang, Q. Liu, W. Yang, Fe,N-modulated carbon fibers aerogel as freestanding cathode catalyst for rechargeable Zn–Air battery, Carbon 187 (2022) 196-206.
[51] H. Zhang, S. Hwang, M. Wang, Z. Feng, S. Karakalos, L. Luo, Z. Qiao, X. Xie, C. Wang, D. Su, Single atomic iron catalysts for oxygen reduction in acidic media: particle size control and thermal activation, Journal of the American Chemical Society 139(40) (2017) 14143-14149.
[52] L. Ye, G. Chai, Z.J.A.F.M. Wen, Zn‐MOF‐74 derived N‐doped mesoporous carbon as pH‐universal electrocatalyst for oxygen reduction reaction, 27(14) (2017) 1606190.
[53] S. Li, T. Mou, G. Ren, J. Warzywoda, Z. Wei, B. Wang, Z. Fan, Gel based sulfur cathodes with a high sulfur content and large mass loading for high-performance lithium–sulfur batteries, Journal of Materials Chemistry A 5(4) (2017) 1650-1657.
[54] M.P. Illa, C.S. Sharma, M. Khandelwal, Catalytic graphitization of bacterial cellulose–derived carbon nanofibers for stable and enhanced anodic performance of lithium-ion batteries, Materials Today Chemistry 20 (2021) 100439.
[55] Y. Yuan, X. Xu, J. Xia, F. Zhang, Z. Wang, Q. Liu, A hybrid material composed of reduced graphene oxide and porous carbon prepared by carbonization of a zeolitic imidazolate framework (type ZIF-8) for voltammetric determination of chloramphenicol, Microchimica Acta 186(3) (2019) 191.
[56] V.K. Bharti, A.D. Pathak, C.S. Sharma, M. Khandelwal, Ultra-high-rate lithium-sulfur batteries with high sulfur loading enabled by Mn2O3-carbonized bacterial cellulose composite as a cathode host, Electrochimica Acta 422 (2022) 140531.
[57] M.D. Walle, M. Zhang, K. Zeng, Y. Li, Y.-N. Liu, MOFs-derived nitrogen-doped carbon interwoven with carbon nanotubes for high sulfur content lithium–sulfur batteries, Applied Surface Science 497 (2019) 143773.
[58] D. Cai, B. Liu, D. Zhu, D. Chen, M. Lu, J. Cao, Y. Wang, W. Huang, Y. Shao, H. Tu, W. Han, Ultrafine Co3Se4 Nanoparticles in Nitrogen-Doped 3D Carbon Matrix for High-Stable and Long-Cycle-Life Lithium Sulfur Batteries, Advanced Energy Materials 10(19) (2020) 1904273.
[59] F.Y. Fan, W.C. Carter, Y.M.J.A.m. Chiang, Mechanism and kinetics of Li2S precipitation in lithium–sulfur batteries, 27(35) (2015) 5203-5209.
[60] Z. Sun, S. Vijay, H.H. Heenen, A.Y.S. Eng, W. Tu, Y. Zhao, S.W. Koh, P. Gao, Z.W. Seh, K.J.A.E.M. Chan, Catalytic polysulfide conversion and physiochemical confinement for lithium–sulfur batteries, 10(22) (2020) 1904010.

[61] W. Hua, H. Li, C. Pei, J. Xia, Y. Sun, C. Zhang, W. Lv, Y. Tao, Y. Jiao, B.J.A.M. Zhang, Selective catalysis remedies polysulfide shuttling in lithium‐sulfur batteries, 33(38) (2021) 2101006.
[62] J. Cho, S. Ryu, Y.J. Gong, S. Pyo, H. Yun, H. Kim, J. Lee, J. Yoo, Y.S. Kim, Nitrogen-doped MoS2 as a catalytic sulfur host for lithium-sulfur batteries, Chemical Engineering Journal 439 (2022) 135568.
[63] P. Wang, B. Xi, M. Huang, W. Chen, J. Feng, S. Xiong, Emerging Catalysts to Promote Kinetics of Lithium–Sulfur Batteries, 11(7) (2021) 2002893.
[64] S. Waluś, C. Barchasz, R. Bouchet, F. Alloin, Electrochemical impedance spectroscopy study of lithium–sulfur batteries: Useful technique to reveal the Li/S electrochemical mechanism, Electrochimica Acta 359 (2020) 136944.
[65] X. Huang, Z. Wang, R. Knibbe, B. Luo, S.A. Ahad, D. Sun, L. Wang, Cyclic Voltammetry in Lithium–Sulfur Batteries—Challenges and Opportunities, Energy Technology 7(8) (2019) 1801001.
[66] G. Zhou, H. Tian, Y. Jin, X. Tao, B. Liu, R. Zhang, Z.W. Seh, D. Zhuo, Y. Liu, J. Sun, Catalytic oxidation of Li2S on the surface of metal sulfides for Li− S batteries, Proceedings of the National Academy of Sciences 114(5) (2017) 840-845.
[67] L. Zhang, M. Ling, J. Feng, L. Mai, G. Liu, J. Guo, The synergetic interaction between LiNO3 and lithium polysulfides for suppressing shuttle effect of lithium-sulfur batteries, Energy Storage Materials 11 (2018) 24-29.
[68] H. Zhao, B. Tian, C. Su, Y. Li, Single-Atom Iron and Doped Sulfur Improve the Catalysis of Polysulfide Conversion for Obtaining High-Performance Lithium–Sulfur Batteries, ACS Applied Materials & Interfaces 13(6) (2021) 7171-7177.
[69] Y. Zhang, J. Liu, J. Wang, Y. Zhao, D. Luo, A. Yu, X. Wang, Z. Chen, Engineering Oversaturated Fe-N5 Multifunctional Catalytic Sites for Durable Lithium-Sulfur Batteries, Angewandte Chemie International Edition 60(51) (2021) 26622-26629.
[70] S. Zhang, X. Ao, J. Huang, B. Wei, Y. Zhai, D. Zhai, W. Deng, C. Su, D. Wang, Y. Li, Isolated Single-Atom Ni–N5 Catalytic Site in Hollow Porous Carbon Capsules for Efficient Lithium–Sulfur Batteries, Nano Letters 21(22) (2021) 9691-9698.
[71] G. Kresse, J. Furthmüller, Efficient iterative schemes for ab initio total-energy calculations using a plane-wave basis set, Physical Review B 54(16) (1996) 11169-11186.
[72] J.P. Perdew, K. Burke, M. Ernzerhof, Generalized Gradient Approximation Made Simple, Physical Review Letters 77(18) (1996) 3865-3868.
[73] S. Grimme, J. Antony, S. Ehrlich, H. Krieg, A consistent and accurate ab initio parametrization of density functional dispersion correction (DFT-D) for the 94 elements H-Pu, The Journal of chemical physics 132(15) (2010) 154104.
[74] P.E. Blöchl, Projector augmented-wave method, Physical review B 50(24) (1994) 17953.
[75] G. Kresse, D. Joubert, From ultrasoft pseudopotentials to the projector augmented-wave method, Physical Review B 59(3) (1999) 1758.
[76] B. Wang, L. Tsetseris, S.T. Pantelides, Introduction of nitrogen with controllable configuration into graphene via vacancies and edges, Journal of Materials Chemistry A 1(47) (2013) 14927-14934.
[77] Z. Luo, R. Nie, V.T. Nguyen, A. Biswas, R.K. Behera, X. Wu, T. Kobayashi, A. Sadow, B. Wang, W. Huang, L. Qi, Transition metal-like carbocatalyst, Nature Communications 11(1) (2020) 4091.
[78] G. Henkelman, B.P. Uberuaga, H. Jónsson, A climbing image nudged elastic band method for finding saddle points and minimum energy paths, The Journal of chemical physics 113(22) (2000) 9901-9904.